A gap design to enable functionalities into nested antiresonant nodeless fiber based systems

Ailing Zhong[1,*], Meng Ding[2], Daniel Dousek[1], Dmytro Suslov[1], Stanislav Zvánovec[1], Francesco Poletti[2], David J. Richardson[2], Radan Slavík[2], and Matěj Komanec[1]

[1] *Department of Electromagnetic Field, Czech Technical University in Prague, Technicka 1902/2, 166 27 Prague 6, Czech Republic*

[2] *Optoelectronics Research Centre, University of Southampton, Southampton, SO17 1BJ, UK*

[*] *zhongail@fel.cvut.cz*

Abstract: By modifying the interconnection design between standard single-mode fiber (SSMF) and nested antiresonant nodeless type hollow-core fiber (NANF), we create an air gap between SSMF and NANF. This air gap enables the insertion of optical elements, thus providing additional functions. We show low-loss coupling using various graded-index multimode fibers acting as mode-field adapters resulting in different air-gap distances. Finally, we tested the gap functionality by inserting a thin glass sheet in between, which formed a Fabry-Perot interferometer and worked as a filter with overall insertion loss of only 0.28 dB.

1. Introduction

Hollow-core optical fiber (HCF) technology has advanced rapidly in the recent years and has become a promising alternative to the ubiquitous standard single-mode fibers (SSMFs). The latest low-loss HCF record of 0.174 dB/km was achieved using double nested antiresonant nodeless fiber (DNANF) [1], which is a significant improvement over nested antiresonant nodeless fiber (NANFs, 0.28 dB/km [2] in 2020 and 0.22 dB/km [3] in 2021). More importantly, this value is at parity with state of the art Ge-doped SSMFs and it is only 0.03 dB away from the state-of-the-art attenuation in Ge-free silica-core optical fiber (~ 0.142 dB/km at 1550 nm) [4]. Encouraged by this impressive progress, the commercialization of the HCF technology has reached early-stage implementation. For example, transmission of 400 Gbit/s over >1000 km of cabled-NANFs in a recirculating loop was recently reported [5].

However, the lack of HCF-based components has been a long-standing challenge when it comes to all-fiber integration and HCF-based networks. In order to enable widespread applications of HCFs, HCF-based couplers, filters, wavelength multiplexers, isolators and other functional components are needed. Furthermore, the HCF-based components should maintain the HCF advantages, i.e. low signal latency [6], low nonlinearity [7], low thermal sensitivity [8] and high damage threshold [9].

To date, most of the research has focused on HCF-based couplers [10–12]. The first hollow-core air-gap antiresonant fiber coupler was demonstrated in 2017 [10], which utilised a dual hollow-core antiresonant fiber structure. Energy transfer was realized between the cores in a sinusoidal pattern along the fiber. The coupling strength can be adjusted by tuning the core diameter and air-gap width. Apart from HCF-based coupler, other HCF-based devices are also under exploration. An HCF-based filter was firstly introduced in 2018 [13], where an antiresonant fiber was heated with a CO_2 laser, which reshaped the fiber structure and resulted in a change in the thickness of the capillary wall, leading to new transmission bands. Nevertheless, this method required delicate control of power and tension to ensure symmetrical heating without any twists or fiber stretching. This method also lacked the possibility of filter tuning.

An alternative approach to HCF-based components is exploiting directly the SSMF-HCF

interconnection which is inevitable in the majority of fiber-optic systems. To provide such a component based on the SSMF-HCF interconnection, an interesting solution was presented in [14] where micro-lensed optics were used to expand, collimate and refocus the beam from SSMF to HCF, thus forming an air gap. The key advantage of this interconnection approach was the possibility to insert optical elements in the air gap and the flexibility of realizing various functions based on the requirements. Functional components such as an HCF-based isolator were demonstrated, with a total loss of 1.5 dB (including 0.53 dB insertion loss when there are no functional elements in the gap, and 0.97 dB additional loss introduced by the isolator).

In this paper, we propose an approach of HCF-based component design without the need for any additional components (such as lenses) in the SSMF-HCF interconnection. We build upon our previous results in interconnecting SSMF and HCFs [15, 16] and focus on the properties of the air gap between SSMF and HCF with the aim of achieving sufficient gap distance to insert functional optical components directly in the SSMF-HCF interconnection. We propose to significantly increase the air-gap distance by replacing the telecom-standard graded-index (GRIN) fibers acting as mode-field adapters with larger-core GRINs that are available commercially. Besides simulations that show the possibility of obtaining air gaps in excess of 2 mm, we also carried out a proof-of-principle experiment in which we increased the air-gap distance sufficiently to insert a 100 µm thick glass sheet. This glass sheet was uncoated in our experiment, consequently showing Fabry-Perot resonances in transmission. In the future, a thin-film filter could be deposited on its surface and the glass sheet could be tilted to tune its central wavelength. The overall insertion loss with the glass sheet inserted was only 0.28 dB and included 0.25 dB insertion loss when there are no functional elements in the gap and 0.03 dB additional loss introduced by the glass-sheet based Fabry-Perot filter.

2. Design principle and simulation

The SSMF-HCF interconnection we previously developed [15] used an OM2 fiber as a GRIN mode-field adapter (MFA), which was spliced to the SSMF. The GRIN fiber was polished to 0.25 pitch length (collimated beam output) as depicted in Fig. 1(a). This allowed almost perfect expansion of the SSMF mode-field to that of an HCF (6-tube NANF in [15]) resulting in the coupling loss of 0.16 dB. What we observed at that time was that the GRIN MFA and the HCF had a lightly reduced loss when we introduced a small (typically 20-60 μm) air gap in between the MFA and HCF. Here, we firstly experimentally investigate in detail how the loss changes with the gap for various MFA lengths. Further, we investigate the impact of the GRIN MFA parameters on the air-gap distance and design the air-gap size to be sufficiently large to enable the insertion of functional elements into it and thus to obtain added functionality at the SSMF-HCF interconnection.

For a GRIN-based MFA shorter than the 0.25 pitch, the output beam diverges. At 0.25 pitch length, the output beam is collimated (Fig. 1a), which is a scenario that was used previously for low-loss SSMF-HCF connection [15]. Once longer than the 0.25 pitch, the beam converges (focuses) first, reaching a beam waist and then starts diverging again. This is advantageous when an increase in the air-gap size is desired (of interest to us) and low loss can be achieved when the beam waist size reaches that of the HCF fundamental mode. This situation is sketched in Fig. 1(b). We denote the distance from the end face of the MFA to the beam waist position (the air-gap size) as the beam waist distance.

Here, we analyze achievable beam waist distances using four types of GRIN fibers with different core sizes, numerical apertures, and refractive index (RI) profiles. These are standard OM2 GRIN fiber from OFS, GRIN100 from YOFC, and two GRIN fibers commercially available from Berkshire Photonics (GRIN200 and GRIN300). The specification of used GRIN fibers are provided in Table. 1 and their measured RI profiles are presented in Fig. 2.

We performed simulations in Synopsys BeamPROP for our four GRIN MFAs. The simulation

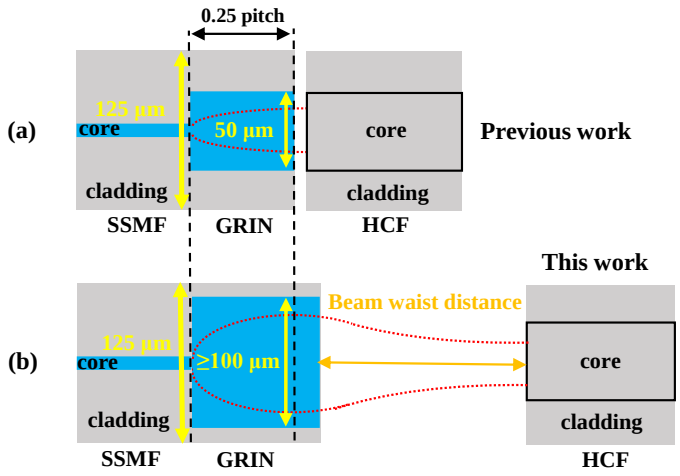

Fig. 1. Beam evolution (red dotted line) (a) when 0.25 pitch GRIN MFA provides ideal mode-field adaptation between the SSMF and the HCF. In [15], this was achieved using GRIN made of OM2 fiber (pictured here). (b) When GRIN provides a larger MFD than the HCF fundamental mode (GRIN100 from YOFC sketched here), it can be made >0.25 pitch long, resulting in output beam focusing, with GRIN length optimized to achieve HCF fundamental mode MFD at the focus and creating here-desired air-gap.

Table 1. Specifications of GRIN fibers.

GRIN fiber type	GRIN OM2	GRIN100	GRIN200	GRIN300
Core diameter (μm)	50	100	200	300
Cladding diameter (μm)	125	125	220	330
Numerical aperture	0.2	0.29	0.22	0.25
Manufacturer	OFS	YOFC	Berk. Photonics	Berk. Photonics

grid size was 1/3 of the computation wavelength (i.e., 0.5 μm). The mode-field first stabilized in the SSMF and subsequently propagated in a sinusoidal pattern in the GRIN segment. We swept GRIN lengths from 0.25 pitch to 0.5 pitch range, in order to estimate how the GRIN length impacts the beam waist distance and corresponding MFDs. The simulation results are presented in Fig. 3.

In Fig. 3(a) we see that the beam waist distance firstly increases with the increased GRIN length, reaching a maximum, and then gradually dropping down to zero when the GRIN length equals 0.5 pitch. The MFD shows a different trend, Fig. 3(b), having maximum MFD at the 0.25 pitch length and then decreasing to ~10 μm (MFD of the used SSMF) at 0.5 pitch.

With respect to the beam waist distance, GRIN200 and GRIN300 can provide up to 2.0 mm and 3.5 mm, respectively. These are large enough to insert optical elements such as isolators or Faraday rotators (e.g., Magnet-free Faraday rotator with a thickness of 420 μm and corresponding optical length of 966 μm at 1550 nm) or a GLB (G series, L-band) isolator with a thickness of 390 μm and corresponding optical length of 920 μm at 1550 nm) [17]. Indeed, the beam waist distance must be larger than the optical length of an inserted element. For GRIN100 based MFA, the maximum beam waist distance is ~230 μm, which enables the insertion of thin elements such as thin glass sheet (e.g., microscopic glass sheets) acting as Fabry-Perot filters or as substrates for

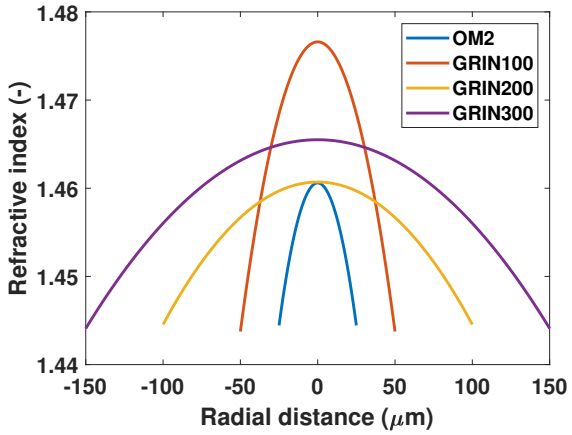

Fig. 2. Measured refractive index profiles of studied GRIN fibers (Table. 1) at 1550 nm.

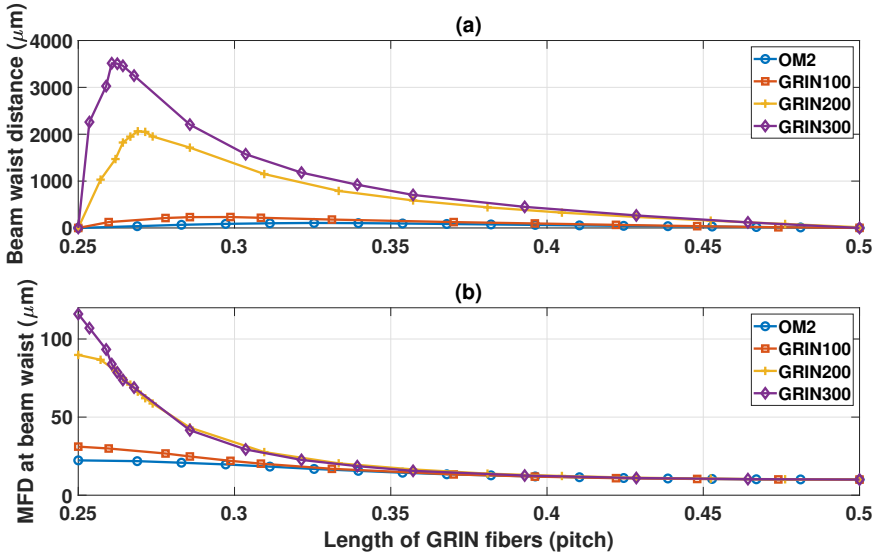

Fig. 3. (a) Beam waist distance, and (b) corresponding MFD, in dependence on the GRIN length for MFAs based on OM2, GRIN100, GRIN200 and GRIN300.

thin-film filters deposited on them.

To obtain low-loss coupling we need the MFD at the beam waist point to be equal to the MFD of the fundamental mode of our HCF. Figure. 4 shows what are the optimal beam waist distances for our 6-tube NANF with MFD of 26.3 μm at 1550 nm that we use in the follow-up experiments. For the OM2-based MFA, the maximum MFD (MFD at 0.25 pitch) is 22.3 μm, which is smaller than that (26.3 μm) of the fundamental mode of our NANF, therefore, the optimum coupling should be obtained when OM2 length is 0.25 pitch and offering no air gap. For GRIN100-based MFA, the MFD at 0.25 pitch is 31.1 μm, decreasing to the target 26.3 μm at GRIN length of ~0.28 pitch, offering an air-gap of 230 μm. For GRIN200- and GRIN300-based MFAs, maximum achievable MFDs are 90 μm and 116 μm, respectively, and the optimum coupling into our HCF should be obtained at beam waist distances of 1.1 mm and 1.7 mm, respectively with GRIN

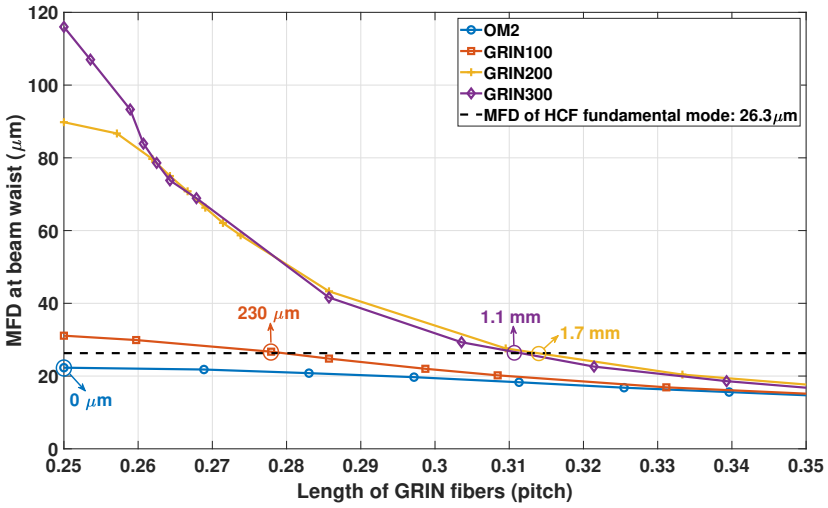

Fig. 4. MFD at beam waist in dependence of GRIN length and comparison of gaps provided by different types of GRIN-based MFAs under optimum coupling.

lengths of ~0.31 pitch for both of them.

In this paper, we decided for proof-of-concept to verify our model on GRIN100-based MFA and compare it with the formerly used OM2-based MFA. GRIN100 has a cladding diameter identical to SSMF and offers a sufficient air gap for the proposed function demonstration.

3. Fabrication and measurement

To verify our simulation results, we have measured the coupling loss dependence on air-gap distance for both OM2- and GRIN100-based MFAs. We prepared a set of OM2-based MFAs with different OM2 lengths (0.25 pitch, 0.30 pitch, 0.31 pitch, 0.32 pitch and 0.37 pitch). For GRIN100-based MFAs, we also prepared a set of samples with GRIN100 lengths of 0.25 pitch, 0.28 pitch, 0.29 pitch, 0.31 pitch and 0.33 pitch. Both sets were prepared without anti-reflective coatings, as the goal was first to find the optimal gap distance.

The experimental setup is presented in Fig. 5. An Erbium-doped fiber amplifier (EDFA) was used as a broadband light source. The signal then passed through an optical bandpass filter (OBPF) narrowing the bandwidth to 1545-1555 nm. After that, the filtered signal was sent to the device under test (DUT), which consisted of an input GRIN-based MFA connected to the HCF, and HCF output was aligned to the output MFA with a fixed gap and it stayed untouched for the whole measurement. As HCF we used a 50 m-long 6-tube nested antiresonant nodeless fiber (NANF [18]) with MFD of 26.3 μm at 1550 nm, the microscope image of our NANF cross-section is presented in Fig. 5. Subsequently, the signal was split via a 3 dB coupler and detected by a power meter (PM, Thorlabs S154C) and an optical spectrum analyzer (OSA, Yokogawa AQ6370).

For precise insertion loss measurement, we first reference our setup by splicing the OBPF output pigtail to the input pigtail of the 3 dB coupler. Then we cut this splice and spliced in our DUT. The insertion loss per interconnection is then calculated as the measured insertion loss minus the HCF loss (0.1 dB) and divided by two. The samples were measured one by one. The air-gap distance was increased from 0 to 280 μm with a step of 20 μm. The results are shown in Fig. 6 for both OM2- and GRIN100-based MFAs. Note, that all the prepared samples are affected by Fresnel losses, which add 0.16 dB/interconnection. This can easily be remedied by an anti-reflective coating.

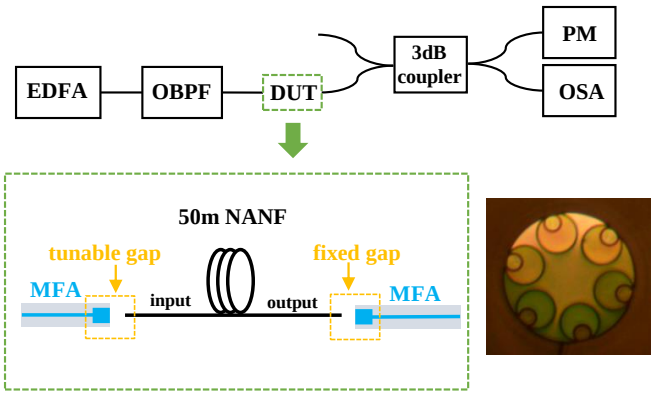

Fig. 5. Experimental setup (EDFA: erbium-doped fiber amplifier, OBPF: optical band-pass filter, DUT: device under test, PM: power meter, OSA: optical spectrum analyzer, MFA: mode-field adapter, NANF: Nested antiresonant nodeless fiber). Insets show DUT detail and microscope image of tested NANF.

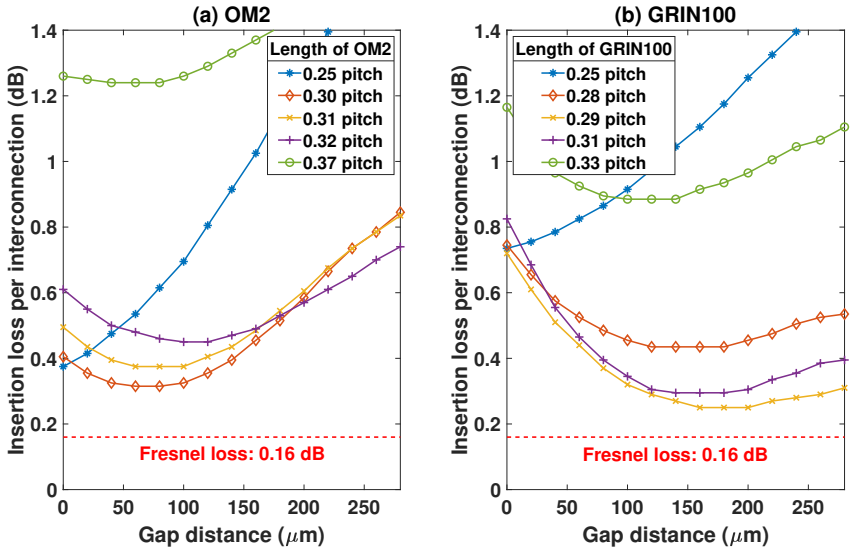

Fig. 6. Insertion loss for a single SSMF-HCF interconnection based on (a) OM2 MFAs and (b) GRIN100 MFAs.

From the results we can see that for GRIN MFA length of 0.25 pitch, the coupling loss increases with the air-gap distance, leading to no gap or a very small air-gap ($\leq$20 μm) between GRIN MFA and HCF. For all GRIN MFA lengths longer than 0.25 pitch, the curves follow the same trend. The coupling loss firstly reduces when we enlarge the air gap, then it reaches a minimum, subsequently, the coupling loss increases again if we further enlarge the air gap. This coupling loss minimum is specific for each particular GRIN MFA and selected HCF, leading to a specific beam waist distance.

For our NANF, the air-gap distances with low-loss coupling achieved for OM2-based MFA and GRIN100-based MFA are 120 µm, and 200 µm, respectively. This correlates well with the simulation results (Fig. 7) of OM2-based MFAs (~6 μm average offset). For GRIN100-based

MFA we see a constant offset (~35 μm) between simulated values and experimental values. We believe this difference is caused by slight imprecision in the measured RI profile of GRIN100.

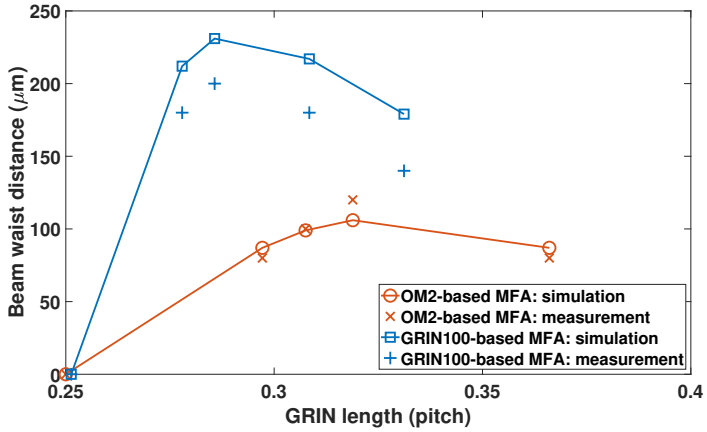

Fig. 7. Comparison of beam waist distances between simulation and measurement provided by OM2-based MFAs and GRIN100-based MFAs.

4. Proof-of-concept demonstration of gap-enabled functionality

The above-achieved gap distance of 200 μm is already sufficient to insert thin functional optical elements, the schematic representation is shown in Fig. 8. For the proof-of-concept, we have chosen a thin glass sheet acting as a Fabry-Perot filter. The experimental setup is the same as shown in Fig. 5, excluding the OBPF, enabling characterization over a broader wavelength range of 1525-1565 nm. We inserted the glass sheet into the gap between the GRIN100-based MFA (0.29 pitch).

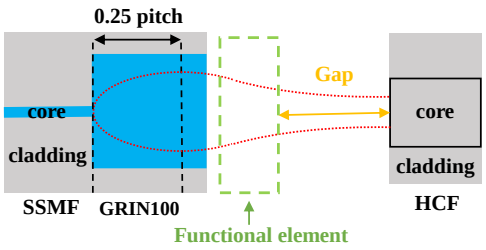

Fig. 8. Schematic representation of our interconnection method to provide additional functionality into HCF-based system.

We conducted the experiments with two types of glass sheets: type #0 (Thorlabs, CG00C2) and type #1.5H (Thorlabs, CG15CH2), with thicknesses of 100 ±15 μm and 170 ±5 μm, respectively. Both of the glass sheets are made from Schott D 263® M Glass, with RI of 1.5058 at 1550 nm. Therefore, the optical thickness of glass sheet for type #0 and type #1.5H are 150 μm and 256 μm, respectively.

To reference the measurement, we first aligned the HCF with both input and output MFAs, then recorded the power and spectrum as a reference. In the next step, we inserted the glass sheet into the gap, aligned the MFA with HCF, then recorded the power and spectrum again. By comparing the power difference, we calculated the additional loss introduced by the glass sheet.

Figure. 9 (a) and (b) illustrate the Fabry-Perot resonance spectrum resulting from the glass sheet type #0 and type #1.5H, respectively.

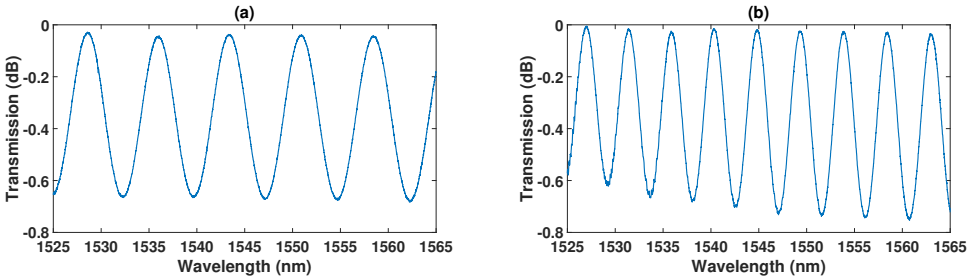

Fig. 9. Transmission spectrum of Fabry-Perot interferometer formed by the precision cover glass (a) #0 (physical thickness: $100 \pm 15\,\mu$m), (b) #1.5H (physical thickness: $170 \pm 5\,\mu$m).

The free spectral range (FSR) of a Fabry-Perot interference can be calculated as:

$$FSR = \frac{\lambda^2}{2nL} \tag{1}$$

where λ is the wavelength of light, n is the RI of the glass sheet and L represents the thickness of the glass sheet. Based on the spectra presented in Fig. 9, we calculated the average FSR, which was 7.25 ± 0.15 nm and 4.56 ± 0.07 nm, respectively. Therefore, the thicknesses ($L = \frac{\lambda^2}{2n \cdot FSR}$) of the glass sheets were $110 \pm 2\mu$m and $175 \pm 3\mu$m respectively, being in good agreement with the expected values of $100 \pm 15\,\mu$m and $170 \pm 15\,\mu$m, respectively.

To analyze the glass sheet performance in detail, we measured the additional insertion loss dependence on gap distance (now with the glass sheet inserted). In this measurement, the glass sheet was at a fixed distance ($\sim 10\,\mu$m) to the MFA and we moved the HCF with a step of $20\,\mu$m. The results are shown in Fig. 10.

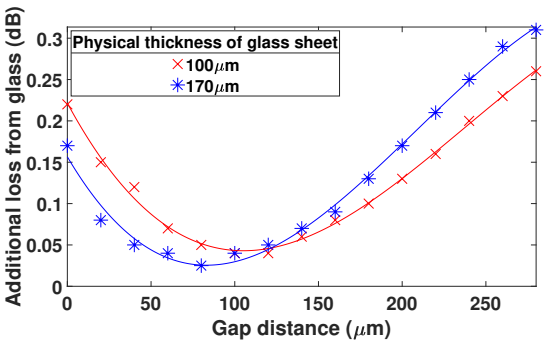

Fig. 10. Additional loss introduced by the glass sheet dependence on gap distance.

The additional loss and low-loss air-gap distance introduced by #0 and #1.5H glass were 0.04 dB, 120 μm and 0.03 dB, 80 μm, respectively. The total insertion loss of the SSMF-GRIN MFA-Glass sheet-HCF system is only 0.28 dB (which could be reduced to as little as 0.12 dB if anti-reflective coating is deposited on the GRIN end-facet, as demonstrated previously [15]).

5. Conclusions

We have demonstrated that by designing the GRIN mode-field adapter, we can modify the beam waist distance (air-gap distance) in an SSMF-HCF interconnection, which enables the insertion of functional optical elements. Through our MFA design, we can create an air gap of predefined length as well as achieve low-loss coupling.

We measured and characterized the gap distances with OM2-based and GRIN100-based MFAs, respectively. With OM2-based MFA, we reached a gap distance of ~120 μm, which can be useful e.g., for gas sensing by allowing a gas inlet/outlet [19]. With GRIN100-based MFA, the optimal gap distance was doubled to around 200 μm, moreover, this gap can be extended to 300 μm at the sacrifice of only 0.06 dB higher insertion loss. The optimal gap distances matched with the simulation predictions of beam waist distances acquired by our MFA models. Furthermore, we also simulated GRIN200 and GRIN300, the gap can be expanded to 1.1 mm by GRIN200 and 1.7 mm by GRIN300, respectively with low-loss coupling to our HCF.

Finally, we demonstrated a Fabry-Perot filter by inserting glass sheets with thicknesses of 100 μm and 170 μm into the SSMF-HCF air gap. We have verified that our design not only provides low-loss interconnection between SSMF and HCF, but also creates a gap to introduce additional functionalities into an HCF-based system. Our design thus provides a versatile and efficient method to build low-loss HCF-based components without complicated adaption and structural alteration of the fiber.

In the future, it will be possible to insert thicker optical components by using GRIN200- and GRIN300-based MFAs, e.g. a Magnet-free Faraday rotator with an optical thickness of 966 μm at 1550 nm or a GLB (G series, L-band) isolator with an optical thickness of 920 μm at 1550 nm [17], which is generally used for in-line optical isolators with only a small increase of the component loss.

6. Acknowledgement

This work was supported by the Czech Science Foundation (GACR) grant GA22-32180S, by the Czech Technical University in Prague project SGS20/166/OHK3/3T/13, by the EPSRC project "Airguide Photonics" under grant EP/P030181/1. F. Poletti gratefully acknowledges EU ERC (grant 682724); R. Slavík was supported by RAEng Fellowship.

References

1. G. T. Jasion, H. Sakr, J. R. Hayes, S. R. Sandoghchi, L. Hooper, E. N. Fokoua, A. Saljoghei, H. C. Mulvad, M. Alonso, A. Taranta *et al.*, "0.174 dB/km Hollow Core Double Nested Antiresonant Nodeless Fiber (DNANF)," in *2022 Optical Fiber Communications Conference and Exhibition (OFC),* (IEEE, 2022), pp. 1–3.
2. G. T. Jasion, T. D. Bradley, K. Harrington, H. Sakr, Y. Chen, E. N. Fokoua, I. A. Davidson, A. Taranta, J. R. Hayes, D. J. Richardson *et al.*, "Hollow core NANF with 0.28 dB/km attenuation in the C and L bands," in *Optical Fiber Communication Conference,* (Optical Society of America, 2020), pp. Th4B–4.
3. H. Sakr, T. D. Bradley, G. T. Jasion, E. N. Fokoua, S. R. Sandoghchi, I. A. Davidson, A. Taranta, G. Guerra, W. Shere, Y. Chen *et al.*, "Hollow core NANFs with five nested tubes and record low loss at 850, 1060, 1300 and 1625nm," in *2021 Optical Fiber Communications Conference and Exhibition (OFC),* (IEEE, 2021), pp. 1–3.
4. Y. Tamura, H. Sakuma, K. Morita, M. Suzuki, Y. Yamamoto, K. Shimada, Y. Honma, K. Sohma, T. Fujii, and T. Hasegawa, "The first 0.14-dB/km loss optical fiber and its impact on submarine transmission," J. Light. Technol. **36**, 44–49 (2018).
5. A. Saljoghei, M. Qiu, S. Sandoghchi, C. Laperle, M. Alonso, M. Hubbard, I. Lang, M. Pasandi, Y. Chen, M. Petrocich *et al.*, "First Demonstration of Field-Deployable Low Latency Hollow-core Cable Capable of Supporting> 1000km, 400Gb/s WDM Transmission," arXiv preprint arXiv:2106.05343 (2021).
6. M. Kuschnerov, B. J. Mangan, K. Gong, V. A. Sleiffer, M. Herrmann, J. W. Nicholson, J. M. Fini, L. Meng, R. S. Windeler, E. M. Monberg *et al.*, "Transmission of commercial low latency interfaces over hollow-core fiber," J. Light. Technol. **34**, 314–320 (2015).
7. Z. Liu, B. Karanov, L. Galdino, J. R. Hayes, D. Lavery, K. Clark, K. Shi, D. J. Elson, B. C. Thomsen, M. N. Petrovich *et al.*, "Nonlinearity-free coherent transmission in hollow-core antiresonant fiber," J. Light. Technol. **37**, 909–916 (2019).

8. R. Slavík, G. Marra, E. N. Fokoua, N. Baddela, N. V. Wheeler, M. Petrovich, F. Poletti, and D. J. Richardson, "Ultralow thermal sensitivity of phase and propagation delay in hollow core optical fibres," Sci. reports **5**, 1–7 (2015).
9. M. Michieletto, J. K. Lyngsø, C. Jakobsen, J. Lægsgaard, O. Bang, and T. T. Alkeskjold, "Hollow-core fibers for high power pulse delivery," Opt. Express **24**, 7103–7119 (2016).
10. X. Huang, J. Ma, D. Tang, and S. Yoo, "Hollow-core air-gap anti-resonant fiber couplers," Opt. Express **25**, 29296–29306 (2017).
11. X. Liu, Z. Fan, Z. Shi, Y. Ma, J. Yu, and J. Zhang, "Dual-core antiresonant hollow core fibers," Opt. express **24**, 17453–17458 (2016).
12. A. Argyros, S. G. Leon-Saval, and M. A. van Eijkelenborg, "Twin-hollow-core optical fibres," Opt. communications **282**, 1785–1788 (2009).
13. X. Huang, K.-T. Yong, and S. Yoo, "A method to process hollow-core anti-resonant fibers into fiber filters," Fibers **6**, 89 (2018).
14. Y. Jung, H. Kim, Y. Chen, T. D. Bradley, I. A. Davidson, J. R. Hayes, G. Jasion, H. Sakr, S. Rikimi, F. Poletti *et al.*, "Compact micro-optic based components for hollow core fibers," Opt. express **28**, 1518–1525 (2020).
15. D. Suslov, M. Komanec, E. R. N. Fokoua, D. Dousek, A. Zhong, S. Zvánovec, T. D. Bradley, F. Poletti, D. J. Richardson, and R. Slavík, "Low loss and high performance interconnection between standard single-mode fiber and antiresonant hollow-core fiber," Sci. Reports **11**, 1–9 (2021).
16. A. Zhong, D. Dousek, D. Suslov, S. Zvánovec, E. N. Fokoua, F. Poletti, D. J. Richardson, R. Slavík, and M. Komanec, "Hollow-core to standard fiber interconnection with customized air-gap distance," in *CLEO: Applications and Technology,* (Optica Publishing Group, 2022), pp. JTh3A–16.
17. GRANOPT, "Faraday rotator (rare-earth iron garnet single crystals)," http://www.granopt.jp/en/product.html. 06/01/2015.
18. F. Poletti, "Nested antiresonant nodeless hollow core fiber," Opt. express **22**, 23807–23828 (2014).
19. D. Suslov, T. W. Kelly, S. Rikimi, A. Zhong, A. Taranta, S. Zvánovec, F. Poletti, D. J. Richardson, M. Komanec, N. Wheeler *et al.*, "Towards compact hollow-core fiber gas cells," in *2022 Conference on Lasers and Electro-Optics (CLEO),* (IEEE, 2022), pp. 1–2.